Pressure-induced semiconductor-to-metal phase transition of a charge-ordered indium halide perovskite

Jia Lin[a,b,1], Hong Chen[a,c,d,1], Yang Gao[e,f,1], Yao Cai[e,f], Jianbo Jin[a], Ahmed S. Etman[g], Joohoon Kang[a,h,i,j,k], Teng Lei[a], Zhenni Lin[e,f], Maria C. Folgueras[e,f], Li Na Quan[a,f], Qiao Kong[a], Matthew Sherburne[a,f], Mark Asta[a,f], Junliang Sun[g], Michael F. Toney[c], Junqiao Wu[e,f,2], and Peidong Yang[a,e,f,h,2]

[a]Department of Chemistry, University of California, Berkeley, CA 94720; [b]Department of Physics, Shanghai University of Electric Power, Shanghai 200090, China; [c]Stanford Synchrotron Radiation Lightsource, Stanford Linear Accelerator Center National Accelerator Laboratory, Menlo Park, CA 94025; [d]School of Environmental Science and Engineering, Southern University of Science and Technology, Shenzhen 518055, China; [e]Department of Materials Science and Engineering, University of California, Berkeley, CA 94720; [f]Materials Sciences Division, Lawrence Berkeley National Laboratory, Berkeley, CA 94720; [g]Department of Materials and Environmental Chemistry, Stockholm University, SE-10691 Stockholm, Sweden; [h]Kavli Energy NanoScience Institute, University of California, Berkeley, CA 94720; [i]Center for NanoMedicine, Institute for Basic Science, Seoul 34126, Korea; [j]Yonsei Institute for Basic Science, Yonsei University, Seoul 34126, Korea; and [k]School of Advanced Materials Science and Engineering, Sungkyunkwan University, Suwon 16419, Korea

Contributed by Peidong Yang, September 21, 2019 (sent for review May 2, 2019; reviewed by Song Jin and Mercouri G. Kanatzidis)

Phase transitions in halide perovskites triggered by external stimuli generate significantly different material properties, providing a great opportunity for broad applications. Here, we demonstrate an In-based, charge-ordered (In^+/In^{3+}) inorganic halide perovskite with the composition of $Cs_2In(I)In(III)Cl_6$ in which a pressure-driven semiconductor-to-metal phase transition exists. The single crystals, synthesized via a solid-state reaction method, crystallize in a distorted perovskite structure with space group *I4/m* with $a = 17.2604(12)$ Å, $c = 11.0113(16)$ Å if both the strong reflections and superstructures are considered. The supercell was further confirmed by rotation electron diffraction measurement. The pressure-induced semiconductor-to-metal phase transition was demonstrated by high-pressure Raman and absorbance spectroscopies and was consistent with theoretical modeling. This type of charge-ordered inorganic halide perovskite with a pressure-induced semiconductor-to-metal phase transition may inspire a range of potential applications.

charge ordered | inorganic | halide perovskite | phase transition | high pressure

Halide perovskites with ABX_3 structure [where A are the alkali elements, such as Cs^+, Rb^+, K^+, $CH_3NH_3^+$ (MA^+), $HC(NH_2)_2^+$ (FA^+); B are Pb^{2+}, Sn^{2+}; X = I^-, Br^-, Cl^-] are of great interest for a wide range of applications, such as photovoltaics, light-emitting diodes, photodetectors, and lasers, due to their remarkable optoelectronic properties (1–7). In addition, their ionic bonding nature with soft metal halide lattices allows abundant phase transition behaviors including lattice distortion, expansion, compression, and rearrangement under various external environmental conditions such as temperature, light, pressure, and electric/magnetic fields (8–13). This type of structural flexibility can lead to significant changes in their optical and electronic properties, and thus further potential opportunities including sensor, memory, and functional window applications (9, 14, 15).

Among the perovskite-type structure materials, spatially charge-ordered (or charge-disproportioned) oxide compounds at A or B site show unique properties, including high-T_C superconducting behaviors, magnetic-field–induced colossal magnetoresistance, and metal–insulator transition (16–20). A few charge-ordered materials have also been explored in halide perovskites, such as Au^+/Au^{3+}, and Tl^+/Tl^{3+}-based compounds. $CsAuX_3$ (X = Cl, Br, I) was demonstrated to show both structural and semiconductor–metal transition at high pressures (21–24). Tl-based compounds ($CsTlF_3$ and $CsTlCl_3$) have been predicted to show high-T_C (~20 K) superconductivity under reasonably high pressures (25, 26). A theory was proposed to interpret the phase transitions in charge-ordered perovskites where the 2 B-site ions with different valence states became indistinguishable under hydrostatic pressures, and a non–charge-ordered state was achieved (27–29).

In this work, we report an In^+/In^{3+}-based charge-ordered halide perovskite compound $Cs_2In(I)In(III)Cl_6$, which shows a semiconductor-to-metal phase transition under high pressures. Although both monovalent In^+ and trivalent In^{3+}-based halide precursors are found to be unstable under ambient conditions, air-stable $Cs_2In(I)In(III)Cl_6$ single crystals can be successfully synthesized through a solid-state reaction method. Optical properties of $Cs_2In(I)In(III)Cl_6$ under a hydrostatic pressure applied by a diamond anvil cell (DAC) were studied. The pressure-induced semiconductor–metal phase transition was observed in both Raman and absorption measurements.

Significance

Metal halide perovskites attract great interest for a wide range of applications due to their remarkable optoelectronic properties. The development of environmentally friendly halide perovskite materials with various crystal structures and compositions offers unprecedented opportunities to achieve desired properties and applications. In this work, we demonstrated an In-based, charge-ordered all-inorganic halide double perovskite with the composition of $Cs_2In(I)In(III)Cl_6$ synthesized by solid-state reaction. High-pressure optical properties were studied, and a pressure-driven, fully reversible semiconductor–metal phase transition was discovered. This In-based charge-ordered structure may inspire new understanding of halide perovskite as well as provide a platform for future discovery of exotic electronic phenomena such as high-T_C superconductivity in halide perovskite compounds.

Author contributions: J.W. and P.Y. designed research; J.L., H.C., Y.G., Y.C., J.J., and A.S.E. performed research; J.L., H.C., Y.G., J.K., T.L., Z.L., M.C.F., L.N.Q., Q.K., M.S., M.A., J.S., and M.F.T. analyzed data; and J.L., H.C., Y.G., and P.Y. wrote the paper.

Reviewers: S.J., University of Wisconsin–Madison; and M.G.K., Northwestern University.

The authors declare no competing interest.

Data deposition: The crystallographic information file (CIF) reported in this paper has been deposited in Inorganic Crystal Structure Database (ICSD), https://icsd.fiz-karlsruhe.de/search (CSD no. 1955021). These data can be obtained free of charge via https://www.ccdc.cam.ac.uk/structures/, or by emailing data_request@ccdc.cam.ac.uk.

[1]J.L., H.C., and Y.G. contributed equally to this work.

[2]To whom correspondence may be addressed. Email: wuj@berkeley.edu or p_yang@berkeley.edu.

This article contains supporting information online at www.pnas.org/lookup/suppl/doi:10.1073/pnas.1907576116/-/DCSupplemental.

Results and Discussion

The charge-ordered $Cs_2In(I)In(III)Cl_6$ (In^+:In^{3+} = 1:1) single crystals were synthesized using a traditional solid-state reaction method. For a typical synthesis, an equivalent molar ratio of $InCl_3$ and InCl was mixed together with 2 equivalent amounts of CsCl, all of which were ground carefully in an Ar glovebox. Afterward, the fine powder was loaded into an evacuated quartz tube. The sealed ampoule was heated at 650 °C for 60 h in a furnace and then slowly cooled down to room temperature. Colorless block-like crystals were harvested as shown in *SI Appendix*, Fig. S1.

Similar to other charge-ordered perovskites such as $CsTlCl_3$ (26), the crystal structure of $Cs_2In(I)In(III)Cl_6$ is very complicated, which requires a comprehensive suite of structural characterization techniques to obtain its accurate crystal structure model. Synchrotron-based single-crystal X-ray diffraction (SCXRD) data obtained at 100 K indicates that there are a set of strong reflection data with weak superreflections in the unwrapped images (*SI Appendix*, Fig. S2). If only considering the strong reflections, we can deduce a tetragonal cell with space group $P4/m$ and a = 5.3915(4) Å, c = 5.5123(6) Å. Based on this analysis, a structure model with a typical perovskite framework with disordered In positions was obtained. However, the simulated powder X-ray diffraction (PXRD) based on this structure model only matches the strongest reflections in the experimental PXRD data, indicating further work is necessary to model the weaker reflections among the strong reflections. Considering the weaker reflections together, a tetragonal supercell with space group $I4/m$ and a = 17.2604(12) Å, c = 11.0113(16) Å can be obtained. Further analysis using rotation electron diffraction (RED) collected from a small piece of nanosized crystal crushed from the bulk crystal also confirmed that this supercell is more suitable for describing the crystal structure of $Cs_2In(I)In(III)Cl_6$ (*SI Appendix*, Fig. S3) (30, 31). As a result, we used this unit cell for data reduction, structure determination, and refinement based on our best SCXRD dataset. The detailed structure parameters are listed in *SI Appendix*, Tables S1 and S2. The final structure refinement turned out to converge successfully with a low R value. The simulated PXRD pattern based on this model well matched the experimental PXRD data (see below for detailed discussion). Energy-dispersive spectroscopy shown in *SI Appendix*, Fig. S4 determined the atomic ratio of Cs:In:Cl to be around 1:0.95:2.99, which was consistent with the double perovskite structure chemical formula.

The final structure model of $Cs_2In(I)In(III)Cl_6$ turns out to be heavily disordered. The structure model shows common structure features as the reported charge-ordered structure of $CsTlCl_3$ and $Cs_{1.17}In_{0.81}Cl_3$ (26, 32), but with its own signature. In our structure model, the In, Cl, and Cs ions are found to be located at disordered positions with various occupancies. Among all of the 4 individual In positions, In(I)3 and In(I)4 are refined to be at a few disordered positions with different occupancies as shown in Fig. 1 *A* and *B*. The exact coordinational polyhedra are hard to be concluded here due to the disorder complexity, as the ionic radius of In(I) is very similar to Cs^+, and significantly different from In(III). The coordination sphere of In(I) with Cl might be more similar to Cs^+ instead of being located as octahedra like $In(III)Cl_6$. As there is a lack of enough accurate statistic experimental data on In(I)–Cl coordinational sphere in both CCDC and ICSD database, here we prefer not to make an absolute conclusion on the In(I)–Cl coordinational sphere, but just use a red ball to represent In(I) position when illustrating our structure model. Unlike the disordered location of In(I), both of the 2 independent In(III) atoms are refined to be located at the ordered positions, while the coordinated Cl atoms around the equatorial plane of the octahedra are all disordered into 2 positions. These disorders introduce the 45° rotation of the $In(III)Cl_6$ octahedra as highlighted in green and yellow in Fig. 1*C*. The partial occupancies of Cl2A/Cl2B, Cl5A/Cl5B, and Cl7A/Cl7B are equal to 0.79/0.21, 0.79/0.21, and 0.77/0.23, respectively. The rotation of the $In(III)Cl_6$ results in 2 disordered structural components as shown in Fig. 1 *D–F* and Fig. 1 *G–I*, with a ratio around 0.78/0.22 as determined by the ratio of disordered Cl atom components. The general crystal structure model of component 1 shown in Fig. 1 *D–F* is very much the same as a double perovskite, while the rotation of the $In(III)Cl_6$ octahedra as highlighted in blue introduces the supercell feature,

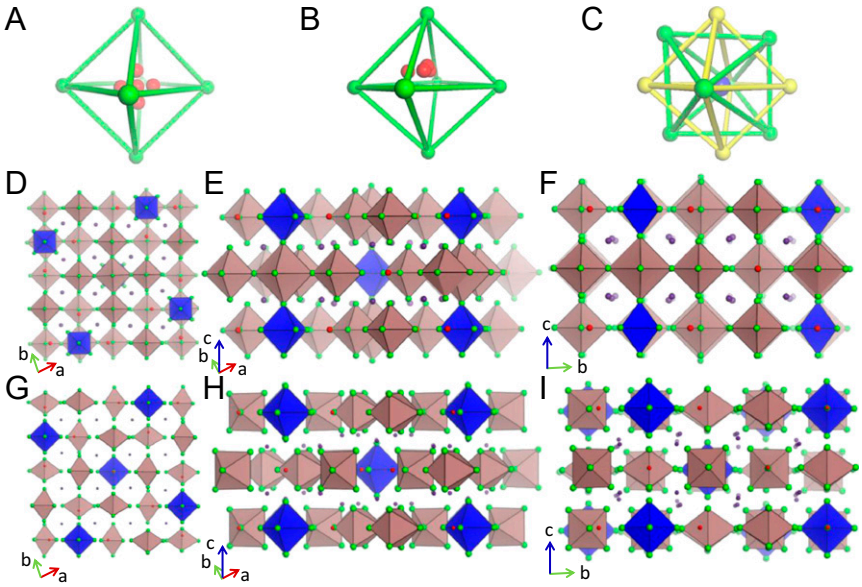

Fig. 1. Single-crystal structure of $Cs_2In(I)In(III)Cl_6$. (*A* and *B*) Disordered In(I)3 (*A*) and In(I)4 (*B*) positions in the $In(I)Cl_6$ octahedra. (*C*) Disordered Cl ion positions around the $In(III)Cl_6$ octahedra. (*D–F*) Disordered component 1 viewing along [001], [110], and [100] zone axis, respectively. (*G–I*) Disordered component 2 viewing along [001], [110], and [100] zone axis, respectively. Color scheme: red balls, In(I) atoms; green and yellow balls, Cl atoms; blue and amber, In(III) atoms; purple, Cs atoms.

which is very similar to the reported $Cs_{1.17}In_{0.81}Cl_3$. The small difference between component 1 and $Cs_{1.17}In_{0.81}Cl_3$ is the atomicity of In(I) position as illustrated with a red ball in the figure. In our structure, based on the comprehensive elemental analysis and refinement results, In(I) positions should be fully occupied with In, while mixed occupancies of Cs^+ and In^+ have been observed in $Cs_{1.17}In_{0.81}Cl_3$. The other 22% of the single crystal is contributed by component 2 resulting from the 45° rotation of the $In(III)Cl_6$ octahedra as shown in Fig. 1 *G*–*I*. In component 2, the structure model is deviated far away from a typical perovskite structure. Although it is not fully understood why the $In(III)Cl_6$ octahedra preferred to be partially disordered with a rotation feature, it should be the reason for the 8-fold-like extra reflection circles in the unwrapped image of the SCXRD pattern (*SI Appendix*, Fig. S2). Moreover, compared with $Cs_{1.17}In_{0.81}Cl_3$, this structure difference actually contributes to the different physical and chemical properties of our material and results in significant differences in the PXRD patterns.

PXRD collected with laboratory source Cu Kα radiation in Fig. 2*A* shows that the experimental result is well consistent with the simulated pattern, indicating that the sample is in a single pure phase. Also, we reproduced the crystal of the reported $Cs_{1.17}In_{0.81}Cl_3$ and find the experimental and simulated PXRD patterns are significantly different from ours (*SI Appendix*, Fig. S5). As most of the In(I)-based halides materials are susceptible to oxidation (33), the structure stability of the as-synthesized $Cs_2In(I)In(III)Cl_6$ was investigated under ambient condition with PXRD, as shown in Fig. 2*B*. The framework of $Cs_2In(I)In(III)Cl_6$ is stable in dry air (relative humidity of 35%) even over 18 d. The air stability is further confirmed by Raman and absorption spectra (*SI Appendix*, Figs. S6 and S7). The air stability is significantly enhanced compared with the reported $Cs_{1.17}In_{0.81}Cl_3$. We have confirmed the stability difference by tracking the PXRD, absorption, and appearance evolution in the same condition as shown in *SI Appendix*, Figs. S8 and S9. Since In^+ can be easily oxidized, and $InCl_3$ is highly hygroscopic, the formation of the charge-ordered perovskite structure could significantly enhance the stability. To investigate the In^+ charge stability, ex situ synchrotron-based soft X-ray photoelectron spectroscopy (SXPS) has been conducted (Fig. 2 *C* and *D*). The results indicate that the surface of the as-synthesized fresh $Cs_2In(I)In(III)Cl_6$ crystal has an In^+/In^{3+} ratio of about 0.55:1, while the sample after exposure in air shows only pure In^{3+}, suggesting that the valence state of In^+ is not stable against oxidation. Although the PXRD peaks indicate that the crystallographic crystalline phase remains the $Cs_2In(I)In(III)Cl_6$ charge-ordered phase, In^+ might have already been oxidized to In^{3+} on the surface, and prevents the framework from collapsing through self-limiting surface oxidation of the crystals (34, 35). This is also consistent with the weaker peak intensity and peak broadening of the PXRD pattern after a few days of air exposure.

Previous studies on the charge-ordered halide perovskites such as $CsAuCl_3$ and $CsTlCl_3$ claimed that the wide bandgap semiconducting properties in these crystals originated from the strong coupling of the charge carriers (25, 29). Herein, we utilize optical and electrical measurements to explore the properties of our $Cs_2In(I)In(III)Cl_6$ crystals. *SI Appendix*, Fig. S10 shows the absorbance spectrum at room temperature, indicating that the material has an optical bandgap of around 3.0 eV. From photoluminescence measurement (*SI Appendix*, Fig. S11), a broad emission peak centered at about 500 nm with very low intensity appears at room temperature. Further lowering the temperature down to 4 K, the emission intensity is increased 2-fold of its original intensity, but still quite broad and weak, indicating poor light-emitting property of the material. Furthermore, electrical characteristics of this crystal were studied via current (*I*)–voltage (*V*) measurements. Symmetric and linear *I*–*V* output characteristics in the dark (I_{dark}), under white-light illumination (I_{light}), and the photocurrent ($I_{ph} = I_{light} - I_{dark}$) are shown in *SI Appendix*, Fig. S12, respectively, indicating the semiconducting behavior of this material without external stress.

To test possible semiconductor-to-metal phase transition of this crystal at high pressures, we explored its optical properties under pressure using a 4-post symmetric DAC coupled with a

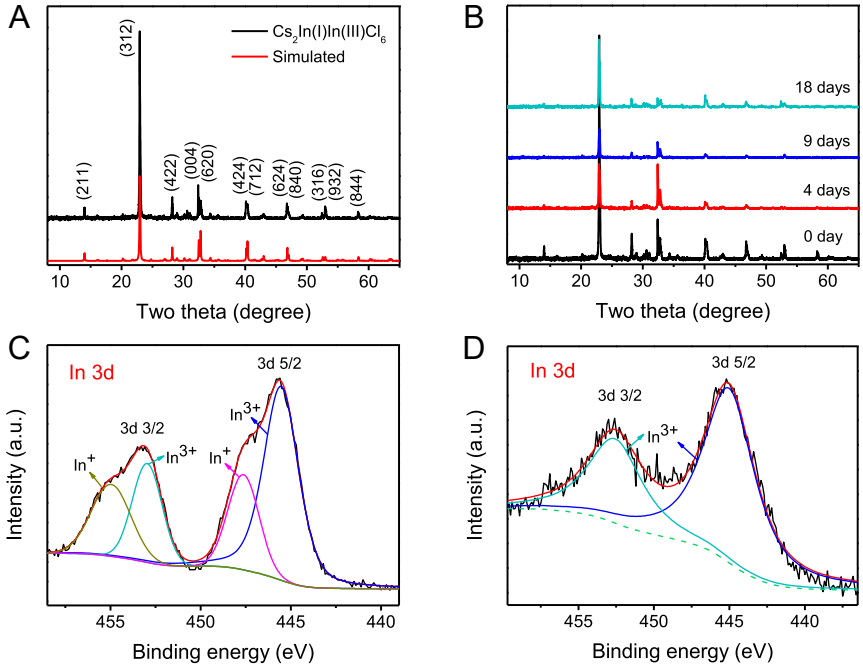

Fig. 2. Structure and valence state stability. (*A* and *B*) PXRD patterns of (*A*) as-synthesized $Cs_2In(I)In(III)Cl_6$ powder and (*B*) that after exposure to air for 0 to 18 d. (*C* and *D*) SXPS of fresh sample and that after exposure to air for 1 d.

hydrostatic pressure medium. DAC has been widely used to investigate the structural and electronic properties of halide perovskites under high pressures (10, 36–41). Raman measurement of $Cs_2In(I)In(III)Cl_6$ at ambient pressure (0 GPa) and room temperature (295 K) showed 1 prominent peak at 279 cm^{-1}, which could be assigned to the In(I)–Cl–In(III) mode (26, 32) and 2 other minor peaks at 143 and 189 cm^{-1} (*SI Appendix*, Fig. S6). The Raman spectra did not show any significant temperature dependence from 295 K down to 77 K (*SI Appendix*, Fig. S13). We then performed pressure-dependent Raman spectroscopy at room temperature. The main Raman peak at 279 cm^{-1} gradually shifts to higher wavenumber with the increase of pressure (Fig. 3*A* and *SI Appendix*, Fig. S14) and experiences an abrupt intensity drop at 13.2 GPa and finally disappears at 21.9 GPa, suggesting a metallic phase at and beyond this pressure. Meanwhile, the 2 minor Raman peaks at lower frequencies were too weak to be detected under high pressure. The Raman peaks fully recover after the pressure is released; hence the phase transition is reversible. As shown in Fig. 3*B*, the Raman peak shifts almost linearly with pressure at a rate of $d\omega/dP = 3.7$ cm^{-1}/GPa before it collapses at about 22 GPa. The integrated area also shows a drastic drop at ∼10 GPa and becomes nondetectable at >22 GPa (10). The Raman vibration modes softening can be regarded as an important evidence of a charge-ordering to non–charge-ordering phase transition (23, 28, 29). To better demonstrate the pressure-induced semiconductor–metal phase transition, pressure-dependent optical absorbance measurement at room temperature has been performed. As shown in Fig. 3*C*, the absorbance spectrum of $Cs_2In(I)In(III)Cl_6$ red shifts with pressure up to 13.9 GPa, above which absorption increases abruptly with a broadband metallic feature. In the raw transmittance spectra (*SI Appendix*, Fig. S15), the transmitted light intensity abruptly drops at 13.9 GPa and remains low up to 34.7 GPa. The pressure-dependent bandgap evolution of $Cs_2In(I)In(III)Cl_6$ is shown in Fig. 3*D*. The bandgap starts at about 2.9 eV under ambient pressure, and then gradually decreases to about 2.0 to 2.1 eV until 13.9 GPa and closes completely under higher pressures. A strong absorption was also observed in $MAPbI_3$ and charge-ordered $CsAuI_3$ at the transition pressure, consistent with the simultaneous electrical conductivity change near the same pressure, suggesting a semiconductor–metal phase transition (10, 27, 28). The good agreement between optical bandgap closure and electrical conductivity change detected in these 2 similar materials implies that experimentally the optical band gap closure is a reliable and robust clue of a metallic phase, especially when combined with Raman spectra change.

The pressure-induced bandgap changes and semiconductor–metal transition of the charge-ordered $Cs_2In(I)In(III)Cl_6$ were further interpreted by density functional theory (DFT) calculations. We built a 5-atom unit cell of perovskite structure with space group *P*4/*m* and a 10-atom unit cell of double perovskite structure with space group *I*4/*m* for the hypothesized non–charge-ordered $CsInCl_3$ (purely In^{2+}) and charge-ordered $Cs_2In(I)In(III)Cl_6$, respectively. The calculated band structure and density of states are shown in *SI Appendix*, Fig. S16. The results show that, without external stress, the charge-ordered perovskite possesses an electronic bandgap of about 2.3 eV, while the non–charge-ordered system lies in a metallic state of 0-eV bandgap. Particularly, under ambient pressure, the charge-ordered semiconducting phase possesses a lower energy than the non–charge-ordered state, suggesting that the charge-ordered phase is the ground state. The calculated bandgap of the charge-ordered phase gets narrower with the increase of pressure and decreases smoothly to 0 eV at around 13 GPa (Fig. 4*A*). As pressure increases, the energies of both non–charge-ordered and charge-ordered phases increase, and the difference between the energies of the 2 phases decreases (Fig. 4*B*). We further analyzed the In–Cl bond length in the 2 phases under increasing pressure (*SI Appendix*, Fig. S17). The length difference between the 2 types of In–Cl bonds in the charge-ordered phase becomes smaller with the increase of pressure and their values approach the In–Cl bond length in the non–charge-ordered phase. The electronic delocalization of the In^+ and In^{3+} centers contributes to the bandgap change and semiconductor-to-metal transition. To summarize, by combining the Raman peaks disappearance, bandgap closure, and DFT simulations, we conclude that the charge-ordered perovskite undergoes a gradual and reversible semiconductor–metal phase transition within the pressure range of 14 to 22 GPa.

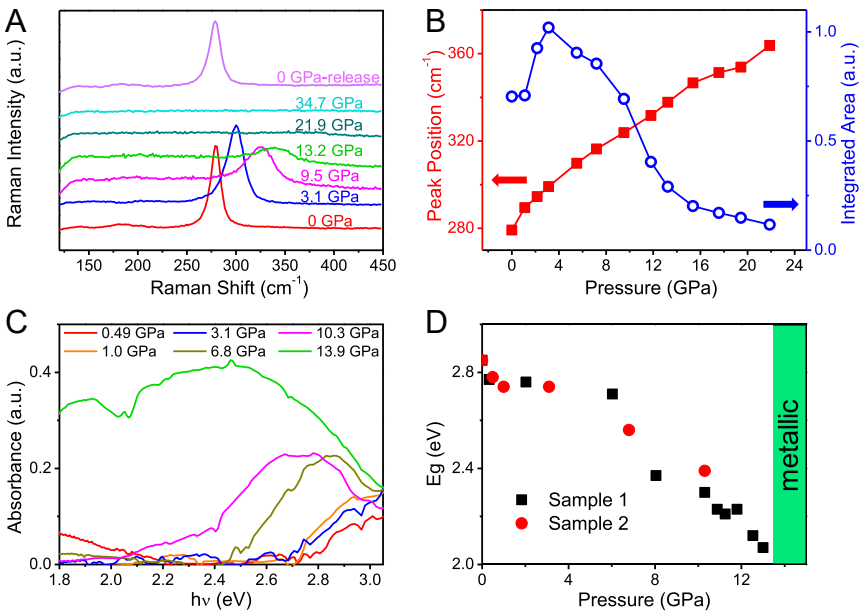

Fig. 3. Semiconductor–metal transition under high pressures. (*A* and *B*) Raman peak blue shifts and intensity (normalized integrated area) weakens with the increase of pressure and disappears completely at about 22 GPa. (*C* and *D*) Absorbance spectra (*C*) and bandgap shrink with the increase of pressure (*D*). After about 14 GPa, a broadband metallic absorption feature appears.

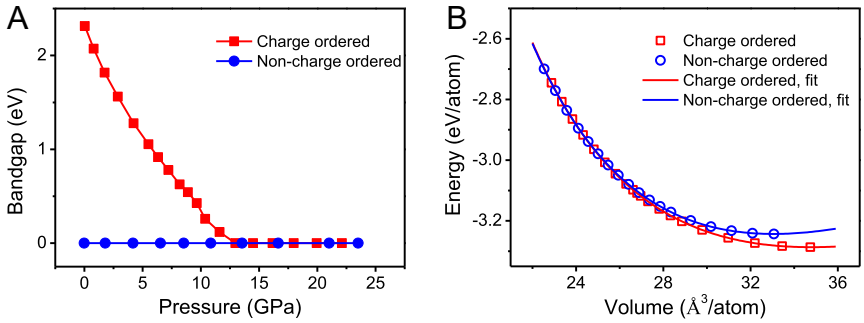

Fig. 4. DFT modeling on the pressure-induced phase transition. (*A* and *B*) Bandgap (*A*) and average energy per atom changes (*B*) of the charge-ordered and non–charge-ordered states at high pressures. The charge-ordered system equilibrium energy (at 0 GPa) is lower than the non–charge-ordered case.

Conclusions

In this work, we have successfully synthesized charge-ordered In-based halide perovskite $Cs_2In(I)In(III)Cl_6$ single crystals by a solid-state reaction method. The structure was characterized by synchrotron-based SCXRD and RED techniques. Although the surface monovalent In^+ ions tend to oxidize in ambient conditions, the bulk single crystals show high structural stability. The intrinsic semiconducting properties were explored via optical and electrical measurements. We further studied high-pressure optical properties and discovered a pressure-driven semiconductor–metal phase transition. The characteristic Raman peak blueshifts with the increase of pressure and disappears completely after about 22 GPa. Its optical bandgap gradually shrinks, and a broadband metallic absorption feature appears after about 14 GPa. Based on the Raman and absorbance spectra, the semiconductor–metal phase transition starts at about 14 GPa and ends completely at about 22 GPa, in agreement with the DFT calculations. Our findings show the great potential of the charge-ordered $Cs_2In(I)In(III)Cl_6$ as a phase transition material with multifunctional properties and a material of high-T_C superconductivity with appropriate doping and high pressure.

Materials and Methods

Single crystals of $Cs_2In(I)In(III)Cl_6$ were synthesized by a solid-state reaction method under vacuum. Synchrotron-based single-crystal X-ray diffraction was performed on a tiny colorless crystal mounted on a Bruker D8 diffractometer equipped with a PHOTON 100 CCD detector with silicon (111) monochromated synchrotron radiation (λ = 0.7288 Å) at 100 K. The crystallographic information file (CIF) has been deposited in the Inorganic Crystal Structure Database under no. 1955021 (42). RED data were collected at 200 K under cryo N_2 atmosphere to confirm the supercell. The valent states of indium atoms in the single crystals were determined by ex situ SXPS. Hydrostatic high-pressure measurements were performed in a DAC. The calculations were carried out employing spin-polarized DFT methods using the projector augmented wave method, as implemented in the Vienna ab initio simulation package. More detailed information regarding the materials and methods are available in *SI Appendix*.

ACKNOWLEDGMENTS. This work was supported by the US Department of Energy, Office of Science, Office of Basic Energy Sciences, Materials Sciences and Engineering Division, under Contract DE-AC02-05CH11231 within the Physical Chemistry of Inorganic Nanostructures Program (KC3103). Simon Teat and Laura McCormick are acknowledged for help on accommodating the single-crystal X-ray beam time. The research used resources at the Stanford Synchrotron Radiation Lightsource at Stanford Linear Accelerator Center National Accelerator Laboratory supported by the US Department of Energy, Office of Science, Basic Energy Sciences under Contract DE-AC02-76SF00515. This research also used resources of the Advanced Light Source, which is a Department of Energy Office of Science User Facility under Contract DE-AC02-05CH11231. The high-pressure experiments were supported by US National Science Foundation Grant DMR-1708448. H.C. acknowledges the postdoctoral scholarship support from the Wallenberg Foundation through the MAX IV synchrotron radiation facility program. J.L. acknowledges the fellowship support from Shanghai University of Electric Power. J.K. acknowledges Institute for Basic Science Global Postdoctoral Fellowship (IBS-R026-D1). The theoretical calculations were supported by the National Research Foundation (NRF), Singapore (CRP NRF2014-NRF-CRP002-036 and NRF-CRP14-2014-03), and the Singapore–Berkeley Research Initiative for Sustainable Energy CREATE Program (Y.C. and M.S.), and the US Department of Energy, Office of Science, Office of Basic Energy Sciences, Materials Sciences and Engineering Division under Contract DE-AC02-05-CH11231 (Materials Project Program KC23MP) (M.A.).

1. M. A. Green, A. Ho-Baillie, H. J. Snaith, The emergence of perovskite solar cells. *Nat. Photonics* **8**, 506–514 (2014).
2. Z.-K. Tan *et al*., Bright light-emitting diodes based on organometal halide perovskite. *Nat. Nanotechnol.* **9**, 687–692 (2014).
3. F. P. G. de Arquer, A. Armin, P. Meredith, E. H. Sargent, Solution-processed semiconductors for next-generation photodetectors. *Nat. Rev. Mater.* **2**, 16100 (2017).
4. S. W. Eaton *et al*., Lasing in robust cesium lead halide perovskite nanowires. *Proc. Natl. Acad. Sci. U.S.A.* **113**, 1993–1998 (2016).
5. Q. Chen *et al*., All-inorganic perovskite nanocrystal scintillators. *Nature* **561**, 88–93 (2018).
6. M. A. Becker *et al*., Bright triplet excitons in caesium lead halide perovskites. *Nature* **553**, 189–193 (2018).
7. H. Zhu *et al*., Lead halide perovskite nanowire lasers with low lasing thresholds and high quality factors. *Nat. Mater.* **14**, 636–642 (2015).
8. M. Lai *et al*., Intrinsic anion diffusivity in lead halide perovskites is facilitated by a soft lattice. *Proc. Natl. Acad. Sci. U.S.A.* **115**, 11929–11934 (2018).
9. J. Lin *et al*., Thermochromic halide perovskite solar cells. *Nat. Mater.* **17**, 261–267 (2018).
10. A. Jaffe, Y. Lin, W. L. Mao, H. I. Karunadasa, Pressure-induced metallization of the halide perovskite $(CH_3NH_3)PbI_3$. *J. Am. Chem. Soc.* **139**, 4330–4333 (2017).
11. E. J. Juarez-Perez *et al*., Photoinduced giant dielectric constant in lead halide perovskite solar cells. *J. Phys. Chem. Lett.* **5**, 2390–2394 (2014).
12. H. Tsai *et al*., Light-induced lattice expansion leads to high-efficiency perovskite solar cells. *Science* **360**, 67–70 (2018).
13. D. Pan *et al*., Visualization and studies of ion-diffusion kinetics in cesium lead bromide perovskite nanowires. *Nano Lett.* **18**, 1807–1813 (2018).
14. Y. Zhao, K. Zhu, Optical bleaching of perovskite $(CH_3NH_3)PbI_3$ through room-temperature phase transformation induced by ammonia. *Chem. Commun. (Camb.)* **50**, 1605–1607 (2014).
15. Y. Niu *et al*., Aggregation-induced emission features of organometal halide perovskites and their fluorescence probe applications. *Adv. Opt. Mater.* **3**, 112–119 (2015).
16. R. Cava *et al*., Superconductivity near 30 K without copper: The $Ba_{0.6}K_{0.4}BiO_3$ perovskite. *Nature* **332**, 814–816 (1988).
17. A. W. Sleight, J. Gillson, P. Bierstedt, "High-temperature superconductivity in the BaPb1-xBixO3 system" in *Ten Years of Superconductivity: 1980–1990*, H. R. Ott, Ed. (Springer, 1993), pp. 257–258.
18. M. Uehara, S. Mori, C. Chen, S.-W. Cheong, Percolative phase separation underlies colossal magnetoresistance in mixed-valent manganites. *Nature* **399**, 560–563 (1999).
19. Y. Tomioka, A. Asamitsu, H. Kuwahara, Y. Moritomo, Y. Tokura, Magnetic-field-induced metal-insulator phenomena in $Pr_{1-x}Ca_xMnO_3$ with controlled charge-ordering instability. *Phys. Rev. B Condens. Matter* **53**, R1689–R1692 (1996).
20. Y. Sakai *et al*., A-site and B-site charge orderings in an s-d level controlled perovskite oxide $PbCoO_3$. *J. Am. Chem. Soc.* **139**, 4574–4581 (2017).
21. R. Keller, J. Fenner, W. Holzapfel, The resistivity of mixed valence compound $Cs_2Au_2Cl_6$ at high pressure and low temperatures. *Mater. Res. Bull.* **9**, 1363–1369 (1974).
22. N. Kojima, M. Hasegawa, H. Kitagawa, T. Kikegawa, O. Shimomura, PT phase diagram and gold valence state of the perovskite-type mixed-valence compounds $Cs_2Au_2X_6$ (X = Cl, Br, and I) under high pressures. *J. Am. Chem. Soc.* **116**, 11368–11374 (1994).
23. X. Liu, K. Matsuda, Y. Moritomo, A. Nakamura, N. Kojima, Electronic structure of the gold complexes $Cs_2Au_2X_6$ (X = I, Br, and Cl). *Phys. Rev. B Condens. Matter Mater. Phys.* **59**, 7925 (1999).
24. S. Wang *et al*., Pressure-induced symmetry breaking in tetragonal $CsAuI_3$. *Phys. Rev. B* **87**, 054104 (2013).
25. Z. Yin, G. Kotliar, Rational material design of mixed-valent high-T_c superconductors. *EPL Europhys. Lett.* **101**, 27002 (2013).

26. M. Retuerto *et al*., Synthesis and properties of charge-ordered thallium halide perovskites, $CsTl^{+}0.5Tl^{3+}0.5X_3$ (X = F or Cl): Theoretical precursors for superconductivity? *Chem. Mater.* **25**, 4071–4079 (2013).
27. N. Kojima, H. Kitagawa, T. Ban, F. Amita, M. Nakahara, Semiconductor-to-metal and metal-to-metal transitions in the three-dimensional mixed-valence compound $Cs_2Au_2I_6$ under high pressures. *Solid State Commun.* **73**, 743–745 (1990).
28. S. Wang *et al*., Bandgap closure and reopening in $CsAuI_3$ at high pressure. *Phys. Rev. B* **89**, 245109 (2014).
29. X. Liu, Y. Moritomo, A. Nakamura, N. Kojima, Pressure-induced phase transition in mixed-valence gold complexes $Cs_2Au_2X_6$ (*X* = Cl and Br). *J. Chem. Phys.* **110**, 9174–9178 (1999).
30. H. Chen *et al*., PKU-3: An HCl-inclusive aluminoborate for Strecker reaction solved by combining RED and PXRD. *J. Am. Chem. Soc.* **137**, 7047–7050 (2015).
31. W. Hua *et al*., A germanosilicate structure with 11×11×12-ring channels solved by electron crystallography. *Angew. Chem.* **126**, 5978–5981 (2014).
32. X. Tan *et al*., Tetragonal $Cs_{1.17}In_{0.81}Cl_3$: A charge-ordered indium halide perovskite derivative. *Chem. Mater.* **31**, 1981–1989 (2019).
33. Z. Xiao *et al*., Intrinsic instability of $Cs_2In(I)M(III)X_6$ (M = Bi, Sb; X = halogen) double perovskites: A combined density functional theory and experimental study. *J. Am. Chem. Soc.* **139**, 6054–6057 (2017).
34. P.-H. Ho *et al*., High-mobility InSe transistors: The role of surface oxides. *ACS Nano* **11**, 7362–7370 (2017).
35. H. Nan *et al*., Producing air-stable InSe nanosheet through mild oxygen plasma treatment. *Semicond. Sci. Technol.* **33**, 074002 (2018).
36. L. Wang, K. Wang, G. Xiao, Q. Zeng, B. Zou, Pressure-induced structural evolution and band gap shifts of organometal halide perovskite-based methylammonium lead chloride. *J. Phys. Chem. Lett.* **7**, 5273–5279 (2016).
37. L. Zhang, Q. Zeng, K. Wang, Pressure-induced structural and optical properties of inorganic halide perovskite $CsPbBr_3$. *J. Phys. Chem. Lett.* **8**, 3752–3758 (2017).
38. Y. Wang *et al*., Pressure-induced phase transformation, reversible amorphization, and anomalous visible light response in organolead bromide perovskite. *J. Am. Chem. Soc.* **137**, 11144–11149 (2015).
39. G. Xiao *et al*., Pressure effects on structure and optical properties in cesium lead bromide perovskite nanocrystals. *J. Am. Chem. Soc.* **139**, 10087–10094 (2017).
40. G. Liu *et al*., Two regimes of bandgap red shift and partial ambient retention in pressure-treated two-dimensional perovskites. *ACS Energy Lett.* **2**, 2518–2524 (2017).
41. H. Zhu *et al*., Pressure-induced phase transformation and band-gap engineering of formamidinium lead iodide perovskite nanocrystals. *J. Phys. Chem. Lett.* **9**, 4199–4205 (2018).
42. J. Lin *et al*., The crystallographic information file (CIF). Inorganic Crystal Structure Database. https://www.ccdc.cam.ac.uk/structures/Search?Ccdcid=1955021. Deposited 21 September 2019.